CsCuCl₃ perovskite compound under extreme conditions

J. S. Rodríguez-Hernández, Mayra A. P. Gómez, O. P. Furtado, D. L. M. Vasconcelos,
A. P. Ayala, and C. W. A. Paschoal[*]
Departamento de Física, Universidade Federal do Ceará, Fortaleza, Ceará, Brazil

Leonardo O. Kutelak, Gustavo A. Lombardi, and Ricardo D. dos Reis
*Brazilian Synchrotron Light Laboratory (LNLS), Brazilian Center for Research in Energy and Materials (CNPEM),
Campinas, São Paulo, Brazil*

Halide perovskites have attracted intense research interest owing to their multifaceted and versatile applications in optoelectronics. This intrigue is further fueled by their propensity to undergo intricate structural modifications under extreme conditions, thereby instigating property changes. Within this context, in this paper, we delve deep into the intricate interplay of structural and vibrational attributes within the inorganic-metal halide perovskite-like CsCuCl₃. Our approach employs Raman spectroscopy and synchrotron powder x-ray diffraction (SPXRD) techniques harnessed under the dual conditions of low temperatures and high pressures (HPs). We have observed a distinct spin-phonon coupling mechanism by employing Raman spectroscopy at low temperatures; this coupling has been manifested as a renormalization phonon phenomenon that occurs notably at $T^* = 15$ K. The correlation between spin and phonon dynamics becomes pronounced through a notable hardening of phonon temperature dependence, a behavior intricately linked to the material antiferromagnetic transition at $T_N = 10.7$ K. SPXRD under HP showed a first-order structural phase transition (SPT) at the critical pressure $P_c = 3.69$ GPa, leading to the transformation from the hexagonal $P6_522$ to a base-centered monoclinic cell. Notably, the coexistence of both phases is discernible within the pressure range from 2.79 to 3.57 GPa, indicating that the SPT involves the reorganization of the internal $[Cu_2Cl_9]^{5-}$ dimer unit, with the Cl-Cu-Cl bending contributing more than stretching modes. Furthermore, we demonstrate that the SPT is reversible, but residual strain pressure influences the modification of the critical pressure P_c value upon pressure decrease.

I. INTRODUCTION

The CsCuX_3 family comprises a class of inorganic-metal halide perovskite compounds with a general chemical formula of AB_yX_s, where A = Rb or Cs; B = Mn, Fe, Co, Ni, or Cu; and X = Cl, Br, or I. These materials have attracted significant attention due to their wide-ranging potential applications in optoelectronics, catalysis, and energy storage [1–4]. Notably, CsCuX_3 compounds exhibit optical and electronic properties like their Pb-based counterparts but offer advantages such as enhanced stability and reduced toxicity compared with lead halides. As a result, there has been growing interest in exploring partial or complete substitution of Cu^{2+} in Pb-based compounds [5–7].

Typically, halide perovskites with the general formula ABX_3 and a transition metal ion B adopt derivatives of the hexagonal perovskite structure [8], giving rise to compounds falling into the Ruddlesden-Popper and Dion-Jacobsen series of materials [9,10]. From a symmetry perspective, the intrinsic threefold or sixfold rotational symmetries lead to frustration in the ordering of magnetic moments or orbital occupancies of the framework ions into a single lowest-energy state at low temperatures, rendering them intriguing, promising candidates for achieving quantum spin-liquid state [11].

Within the CsCuX_3 family, CsCuCl₃ is a perovskite-like material with an antiferromagnetic (AFM) order below $T_N = 10.7$ K (Cu^{2+}: $S = \frac{1}{2}$) [12–14]. The AFM state arises from the exchange interaction within the intrachain and the antisymmetric exchange [Dzyaloshinskii-Moriya (DM)] interaction, allowed by the 120° twist in the AFM phases along the [001] direction [15]. At room temperature, CsCuCl₃ adopts a polytype distorted hexagonal perovskite structure belonging to chiral space group $P6_522$ or $P6_122$, which undergoes a structural phase transition (SPT) at high temperatures (423 K) due to the Jahn-Teller effect, leading to the space group $P6_3/mmc$ [16]. The hexagonal phase $P6_522$ (commonly referred to as left-handed spin-rotation direction) consists of two face-shared distorted $[CuCl_6]^{4-}$ octahedra forming a $[Cu_2Cl_9]^{5-}$ dimer unit, which displays a one-dimensional chain of dimers along the c axis, with the Cs^+ ion occupying the void space between the chains (see Fig. S1 in the Supplemental Material [17]).

The investigation of frustrated quantum many-body systems, such as CsCuCl₃, under high pressure (HP) provides an excellent opportunity to explore the effects of competing interactions at low-energy states. External pressure manipulation in frustrated quantum materials facilitates the active modulation of quantum correlations across classical

*paschoal.william@fisica.ufc.br

and quantum-mechanical regimes, opening doors to studying exotic phenomena emerging in the crossover between these two regimes [18]. The magnetic diagram of $CsCuCl_3$ at low temperatures, as a function of the longitudinal magnetic field ($\mathbf{H} \parallel c$), exhibits a quantum-phase transition ($\mathbf{H} = 12.5$ T) from an umbrella phase to a 2-1 coplanar phase as the magnetic field increases. Similarly, applying pressure increases the incommensurate (IC) wavenumber with the magnetic field and pressure, enhancing neighboring spins and modifying the magnetic diagram through the enhanced DM interaction [19,20]. Consequently, pressure-induced quantum phases are observed, distinguished by the ICN notation (with N ranging from 1 to 5 for each phase), advancing the scientific understanding of controlling quantum mechanical correlations in weakly coupled spin-chain materials through external pressure in $CsCuCl_3$ [21].

Furthermore, the coupling between spin, charge, lattice, and orbital degrees of freedom is fundamental in condensed matter physics, giving rise to emergent phenomena and applications, such as multiferroics and spintronics [22]. Recent interest has grown in exploring spin-phonon coupling (SPC) in materials, which simultaneously control magnetic and phononic properties [23,24]. The stability of magnetic states can be influenced by modifying epitaxial strains or displacing magnetic ions in the sample through external conditions, such as high magnetic fields, HP, or low temperatures. The Hamiltonian governing spin-related phenomena in solids can be expressed as a sum of isotropic exchange (IE), DM, anisotropic exchange (AE), and single-ion anisotropy (SIA) interactions [25,26], given by

$$H_{\text{spin}} = \sum_{ij}^{nn} [J_{\text{IE}}(\mathbf{S}_i \cdot \mathbf{S}_j) + \mathbf{D}_{ij} \cdot (\mathbf{S}_i \times \mathbf{S}_j) + \mathbf{S}_i \cdot \mathbf{\Gamma}_{ij} \cdot \mathbf{S}_j]$$
$$+ A \sum_i (\mathbf{n}_i \cdot \mathbf{S}_i)^2. \tag{1}$$

Here, J_{IE}, $\mathbf{D}_{ij}$, $\mathbf{\Gamma}_{ij}$, and A are the coefficients for IE, AE, DM, and SIA interactions, respectively, while $\mathbf{n}_i$ is the vector direction axis, and $\mathbf{S}_i$ and $\mathbf{S}_j$ denote neighboring spins at sites i and j. These spin interactions are highly dependent on Coulomb interactions, but the terms J_{IE}, $\mathbf{D}_{ij}$, $\mathbf{\Gamma}_{ij}$, and A are dynamically modified by lattice vibrations, leading to SPC and the observed renormalization of phonon frequencies in certain cases [27].

Despite extensive investigations into the magnetic properties of $CsCuCl_3$ at low temperatures and HPs, no systematic study of SPTs or SPC in this crystal has been conducted. Therefore, this paper aims to bridge this gap by reporting on the presence of SPC in $CsCuCl_3$ during the low-temperature AFM phase transition and a first-order HP-induced SPT.

II. EXPERIMENTAL AND COMPUTATIONAL METHODS

Dark red needles of $CsCuCl_3$ single crystals were grown through the slow evaporation method from a solution containing stoichiometric amounts of CsCl and $CuCl_2$ in acidic HCl (47 wt. % in H_2O). The solution was heated at $120°$ C for 1 h and then kept at room temperature in a beaker sealed with paraffin film. The crystals were collected and cleaned with toluene.

The crystal structure was confirmed using single-crystal x-ray diffraction (SCXRD) measurements performed on a Bruker D8 Venture x-ray diffractometer equipped with a Photon II Kappa detector and Mo K radiation ($\lambda = 0.71073$ Å) microfocus source. The crystal was chosen and mounted on a MiTeGen MicroMount using immersion oil. APEX 4 software was used for the unit cell determination and data collection. The data reduction and global cell refinement were made using the Bruker SAINT$^+$ software package, and a multiscan absorption correction was performed with SADABS [28,29]. The structure was solved by intrinsic phasing using SHELXT [30] and refined by least squares on SHELXL [31] included in Olex^2 [32]. The crystallographic illustrations were prepared in Mercury [33] and VESTA software [34]. The determined crystal structure belongs to the $P6_522$ space group with $a = 7.2168$ (1) Å and $c = 18.1853$ (5) Å as cell parameters, consistent with Cui *et al.* [35]. Some verified crystals were crushed to prepare a powder sample with 10 μm thickness, which was used for the measurements at extreme conditions.

Low-temperature Raman spectra of the powder sample were collected using a T64000 Jobin-Yvon spectrometer equipped with an Olympus microscope and an LN_2-cooled charge-coupled device to detect the scattered light. The slits in our measurement setup were taken to get better than $1\,\text{cm}^{-1}$ resolution. The spectra were excited with an argon ion laser ($\lambda = 568$ nm), and the temperature-dependent spectra were obtained using a He-compressed closed-cycle cryostat with precise temperature control (± 0.1 K). To reduce the gradient between the cold finger and the sample, we wait at least 10 min after reaching the target temperature. During this step, the laser spot was kept in the sample to ensure stability under all the measurements, which did not change along the measurement. During this step, the laser spot was kept in the sample to ensure stability under all the measurements, which did not change along the measurement. A membrane diamond anvil cell (DAC) chamber was utilized for pressure-dependent spectra, and Nujol served as the pressure-transmitting medium. The pressure was determined using the ruby pressure [36]. The powder of $CsCuCl_3$ and the ruby were together in the gaskets without contact. Each Raman spectrum was deconvoluted into the sum of Lorentzian functions using FITYK [37].

The HP synchrotron powder x-ray diffraction (SPXRD) data were obtained at the Extreme Methods of Analysis (EMA) beamline of the Brazilian Synchrotron Light Laboratory. These measurements were conducted at ambient temperature, utilizing a monochromatic, 25.514 keV, x-ray beam. HP was generated using a DAC fitted with 600 μm diamond anvils. We used a stainless-steel gasket with a 200 μm hole into which the sample was loaded, along with a ruby ball. Neon was used as the pressure medium. The pressure was determined *in situ* by measuring the wavelength of the ruby fluorescence second peak and was controlled via a gas-membrane mechanism integrated with the DAC. We employed an x-ray spot size of $15 \times 15\,\mu$m at the sample position for the SPXRD measurements. The two-dimensional diffraction images were captured in a transmission geometry using a MARCCD165 detector, which has a pixel size of $73.2 \times 73.2\,\mu$m. Subsequently, these images were processed and integrated using Dioptas 4.0 software [38]. To ensure accuracy, we calibrated the detector distance and other
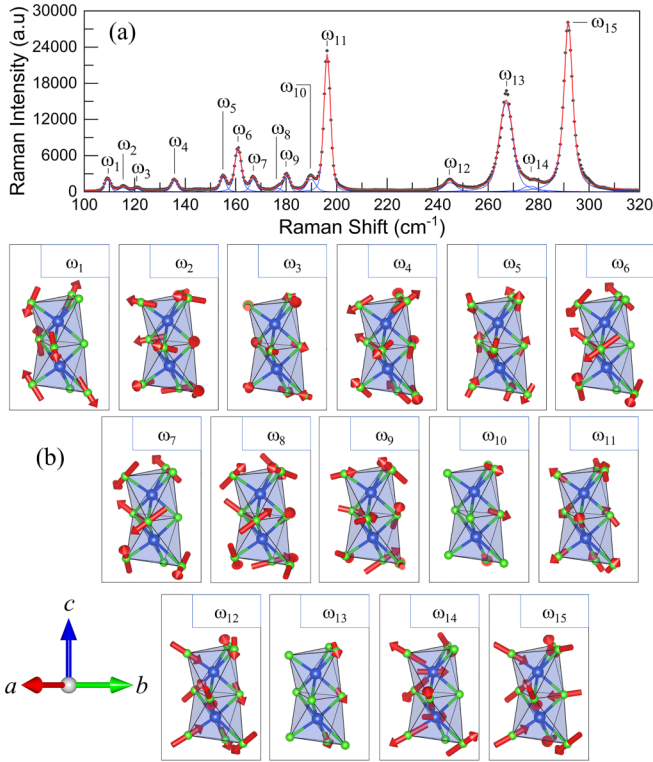
FIG. 1. (a) Raman spectrum of CsCuCl$_3$ at 9.2 K (blue and red curves are the Lorentzian oscillator phonons bands and the total modes convolution, respectively). (b) Calculated Raman modes in CsCuCl$_3$. Note that the dimer unit [Cu$_2$Cl$_9$]$^{5-}$ is described along the a, b, and c directions.

geometrical parameters using the National Institute of Standards and Technology standard reference material 660c (LaB$_6$). The x-ray diffraction (XRD) powder data was indexed and fitted by the Le Bail method [39] with EXPO2014 [40] to obtain the lattice parameters.

Theoretical phonon calculations were performed using density functional theory (DFT) implemented in the QUANTUM ESPRESSO package [41,42]. The calculations included structural optimization using SG15 optimized norm-conserving Vanderbilt pseudopotentials [43], followed by Γ-point phonon calculations. The phonon frequencies were calculated using density functional perturbation theory (DFPT), with the exchange-correlation term determined within the generalized gradient approximation parameterized by Perdew-Burke-Ernzerhof [44]. Additionally, the local density approximation was employed for the exchange-correlation term for Raman intensity calculations.

III. RESULTS AND DISCUSSIONS

A. Typical Raman spectrum and phonon assignments

The group-theory analysis based on the site occupation of CsCuCl$_3$ yields 35 Raman-active phonon modes at room temperature, which are distributed among the irreducible representations of the point group 622 as the direct sum $\Gamma_{\mathrm{RAMAN}} = 6A_1 \oplus 15E_2 \oplus 14E_1$ (see Table SI in the Supplemental Material [17]). Figure 1(a) shows the Raman spectrum

in the 100–320 cm^{-1} range for the CsCuCl$_3$ powder sample at 9.2 K. Since CsCuCl$_3$ does not undergo any SPT at low temperatures, this is the typical spectrum of CsCuCl$_3$ ($P6_522$ symmetry; see Fig. S2 in the Supplemental Material [17], which shows the Raman spectrum at room temperature). The phonon assignments were based on the stable lattice dynamics calculated around the Γ point using DFPT. The DFPT calculations relax the crystallographic cell size and shape by minimizing all quantum forces in the static lattice, which approximates the crystal structure to $T = 0$ K.

Table I summarizes the experimental Raman (300 and 9.2 K) and respective DFPT-calculated phonons, which were compared with previous Raman or IR measurements of similar materials such as ABCl$_3$ ($A = $ Cs, Rb; $B = $ Mn, Co) [45–47], CsBBr$_3$ ($B = $ Co, Mg, Cd) [48], Cs$_2X$Cl$_4$ ($X = $ Cu, Co) [49,50], and [(CH$_3$)$_4$N]$_2$MnX_4 ($X = $ Cl, Br) [51]. These phonons were separated into Cl-Cu-Cl bending and Cl-Cu-Cl stretching. Such calculated phonons are shown in Fig. 1(b), which are described around the [Cu$_2$Cl$_9$]$^{5-}$ dimer unit. A full list of the calculated phonons is given in Table SII in Supplemental Material [17].

B. Raman spectroscopy at low-temperatures in CsCuCl$_3$: SPC

As was previously described, CsCuCl$_3$ exhibits an AFM ordering at $T_N = 10.7$ K produced by the DM interaction, which is allowed by the twist of the [Cu$_2$Cl$_9$]$^{5-}$ dimer unit along the [001] direction [14,52]. This magnetic ordering could induce a SPC in CsCuCl$_3$. To investigate such a coupling, we performed low-temperature Raman spectroscopy. The temperature-dependent Raman spectra of CsCuCl$_3$ in the low-temperature range from room temperature down to 9.2 K are shown in Fig. 2. As discussed before, the material does not exhibit a SPT within the temperature range investigated. In the absence of a SPT, the behavior of the phonon frequency (ω) and the full width at half maximum (FWHM = Γ) can be described by the Balkanski model, which is given by the following equations:

$$\omega(T) = \omega_0 + C\left[1 + \frac{2}{e^x - 1}\right]$$
$$+ D\left[1 + \frac{3}{e^y - 1} + \frac{3}{(e^y - 1)^2}\right], \quad (2)$$

and

$$\Gamma(T) = A\left[1 + \frac{2}{e^x - 1}\right] + B\left[1 + \frac{3}{e^y - 1} + \frac{3}{(e^y - 1)^2}\right], \quad (3)$$

where A, B, C, and D are constants referring to the strength of the anharmonic contributions, and ω_0 is the zero-temperature frequency of the corresponding vibrational mode without spin-phonon interaction. To simplify the analysis, the dimensionless parameters $x = \hbar\omega_0/2k_BT$ and $y = \hbar\omega_0/3k_BT$ were also used in these equations. The fit of the experimental data of the Raman mode parameters by Eqs. (2) and (3) (see Fig. S3 in the Supplemental Material [17]) allows for a detailed description of the paramagnetic phase ($T > 15$ K) of CsCuCl$_3$, with the values of the anharmonic contributions for each mode summarized in Table SIII in the Supplemental Material [17].

TABLE I. Experimental Raman modes (Exp.) at room pressure (300 K), low temperature (9.2 K), and DFPT-calculated phonon frequencies in $CsCuCl_3$. The corresponding lattice constants are $a = b = 7.19$ Å and $c = 18.08$ Å. The modes were given for the wave vector at the Γ point in the Brillouin zone.

Mode frequency	Mode sym. (R)	Exp. (300 K), (cm^{-1})	Exp. (9.2 K), (cm^{-1})	DFPT (cm^{-1})	Vibrational assignment
ω_1	E_1		109	105.8	δ_{as} (Cl-Cu-Cl) str.
ω_2	E_2		115	116.1	δ_s (Cl-Cu-Cl) str.
ω_3	E_2	115	121	122.3	τ (Cl-Cu-Cl) wk. [44,47–49]
ω_4	E_2	132	136	138.1	ω (Cl-Cu-Cl) str. [47–49]
ω_5	E_2		145	152.6	ρ (Cl-Cu-Cl) str.
ω_6	E_1		155	156.8	γ (Cl-Cu-Cl) str.
ω_7	A_1	155	161	160.9	γ (Cl-Cu-Cl) str. [44,47,49]
ω_8	E_1		167	164.0	ω (Cl-Cu-Cl) str.
ω_9	E_2	177	180	175.5	τ (Cl-Cu-Cl) str. [44,47]
ω_{10}	E_2		190	191.4	ν (Cu-Cl) wk.
ω_{11}	E_1	191	196	210.3	ν_s (Cl-Cu-Cl) wk. [44,47]
ω_{12}	A_1	242	245	245.9	ν_s (Cl-Cu-Cl) str. [44,47–49]
ω_{13}	E_1	265	267	266.4	ν_{as} (Cl-Cu-Cl) wk. [44,47–49]
ω_{14}	A_1		276	267.4	ν_{as} (Cl-Cu-Cl) str.
ω_{15}	E_2	286	292	273.7	ν_s (Cl-Cu-Cl) str. [44,47–49]

Abbreviations: δ: bending; τ: twisting/torsion; ω: wagging; ρ: rocking; γ: scissoring; ν: stretching; as: asymmetric; s: symmetric; str.: strong; wk.: weak.

The phonons depicted in Fig. 3 exhibit anomalies in both $\omega(T)$ and $\Gamma(T)$ around $T^* = 15$ K. A sudden phonon hardening is observed at T^* and remains until the AFM transition temperature $T_N = 10.7$ K. Below T_N, the Raman modes exhibit a noticeable softening. Notably, T^* introduces a low-temperature correlation within the system unrelated to any unusual lattice distortion, electronic phase transition, or reported structural/magnetic phase transition in the compound. This intriguing outcome strongly suggests the presence of SPC in $CsCuCl_3$, manifested by the alteration of both mode parameters (frequency and FWHM) through phonon renormalization [53]. While these frequency shifts are typically subtle, often on the order of 1 cm^{-1} or smaller, their systematic nature lends robustness to the findings.

The role of spin-phonon interaction can be elucidated through the static spin-spin correlation average, represented as $\Delta\omega = \omega - \omega_0 = \lambda\langle \mathbf{S}_i \cdot \mathbf{S}_j \rangle$, where λ is the coupling constant, and $\langle \mathbf{S}_i \cdot \mathbf{S}_j \rangle$ denotes the correlation between the neighboring spins in the i and j sites [54–56]. Consequently, at $T > T^*$ (paramagnetic phase), the $\langle \mathbf{S}_i \cdot \mathbf{S}_j \rangle$ term is null due to the absence of the spin ordering. However, in the temperature range $T_N < T < T^*$, a distinct mode frequency renormalization is
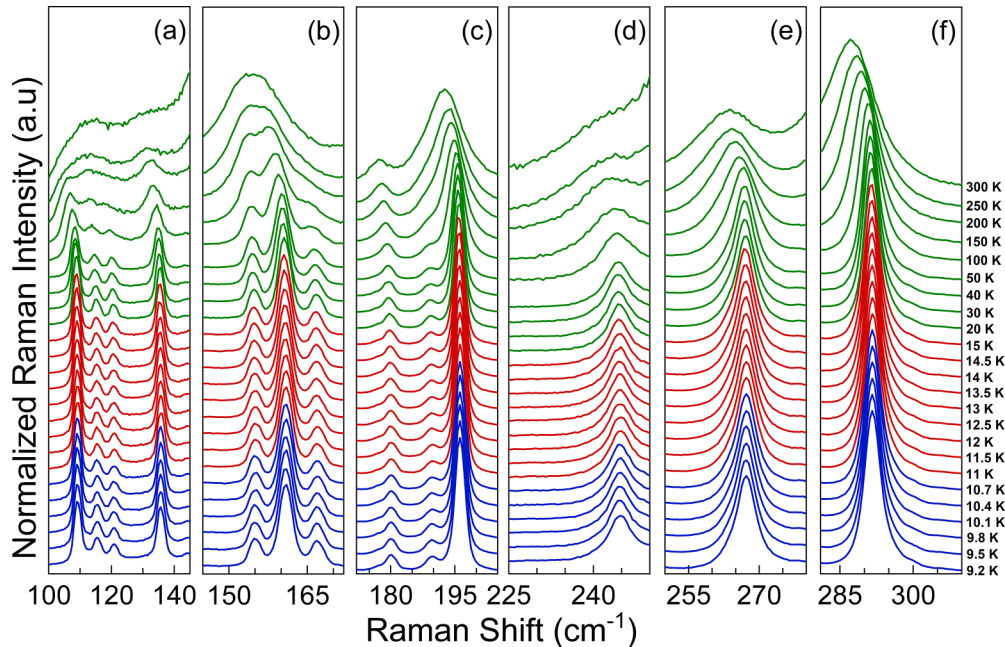

FIG. 2. Temperature-dependent Raman spectra of $CsCuCl_3$ in the ranges (a) $100-145$ cm^{-1}, (b) $145-175$ cm^{-1}, (c) $175-225$ cm^{-1}, (d) $225-250$ cm^{-1}, (e) $250-280$ cm^{-1}, and (f) $280-310$ cm^{-1}.
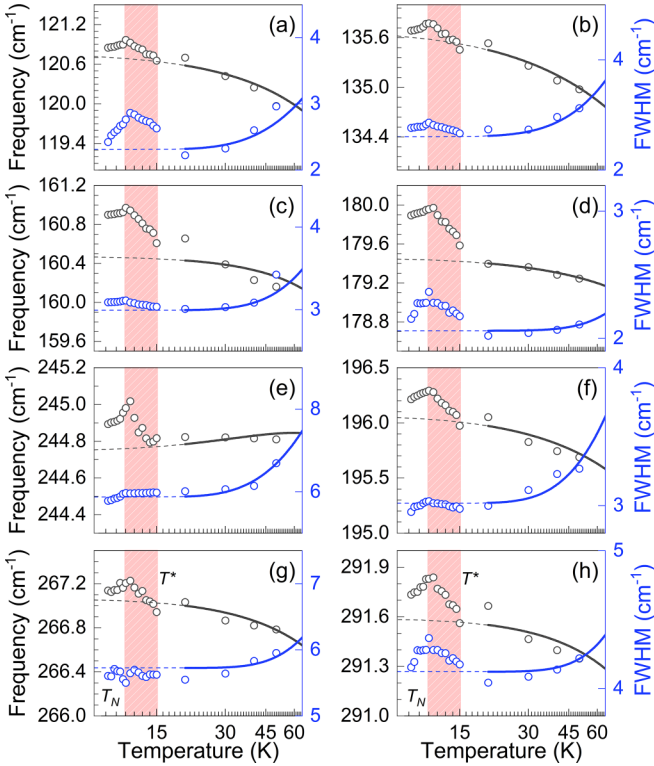
FIG. 3. Temperature dependence of the phonon frequencies (left axes) and full width at half maximum (FWHM; right axes) for selected phonons in the paramagnetic and antiferromagnetic phases. Solid curves are the fits using Eqs. (2) and (3). The orange area describes an anomalous hardening region ($T_N = 10.7$ K $< T < T^* = 15$ K) for (a) ω_3, (b) ω_4, (c) ω_7, (d) ω_9, (e) ω_{11}, (f) ω_{12}, (g) ω_{13}, and (h) ω_{15} phonons.

FIG. 4. Temperature dependence from the anharmonic behavior of selected phonon as a function of $[M(T)/M_0]^2$ for (a) ω_3, (b) ω_4, (c) ω_7, (d) ω_9, (e) ω_{11}, (f) ω_{12}, (g) ω_{13}, and (h) ω_{15} phonons (purple, blue, and red are linear guides for the eyes separated for each region).

already discernible prior to T_N. This observation indicates unconventional magnetic correlations (local spin fluctuations, frustration, or quantum phase, for example) occurring in CsCuCl$_3$ preceding the onset of AFM ordering. Analogous behavior has been reported in AFM RMn$_2$O$_5$ (R = Bi, Eu, Dy) compounds [57,58].

The magnetic order may couple to the phonon frequencies through modulation of the DM interaction parameter. However, for $T_N < T$, the contribution of the softening is driven by the AFM effect. Therefore, it is convenient to estimate the magnetic contribution to the renormalization of the phonon frequency as a function of $\Delta\omega$. The easiest way to do this is by estimating the $\Delta\omega$ dependence with the mean-field approach $((\langle S^z \rangle)/S)^2$ described by the molecular-field approximations mechanism as $[M(T)/M_0]^2$, where $M(T)$ is the temperature dependence of magnetization, and M_0 is the magnetization at zero temperature [59,60].

To obtain $[M(T)/M_0]^2$, we employed the Yamamoto *et al.* [21] longitudinal susceptibility ($\chi_{\parallel}$) data at low temperatures obtained by the authors at $H = 1$ T. Thus, based on the SPC mechanism proposed by Granado *et al.* [61], the phonon renormalization induced by the SPC could be reduced as

$$\Delta\omega = \omega - \omega_0 = \lambda \langle \mathbf{S}_i \cdot \mathbf{S}_j \rangle \propto \left[\frac{M(T)}{M_0} \right]^2. \quad (4)$$
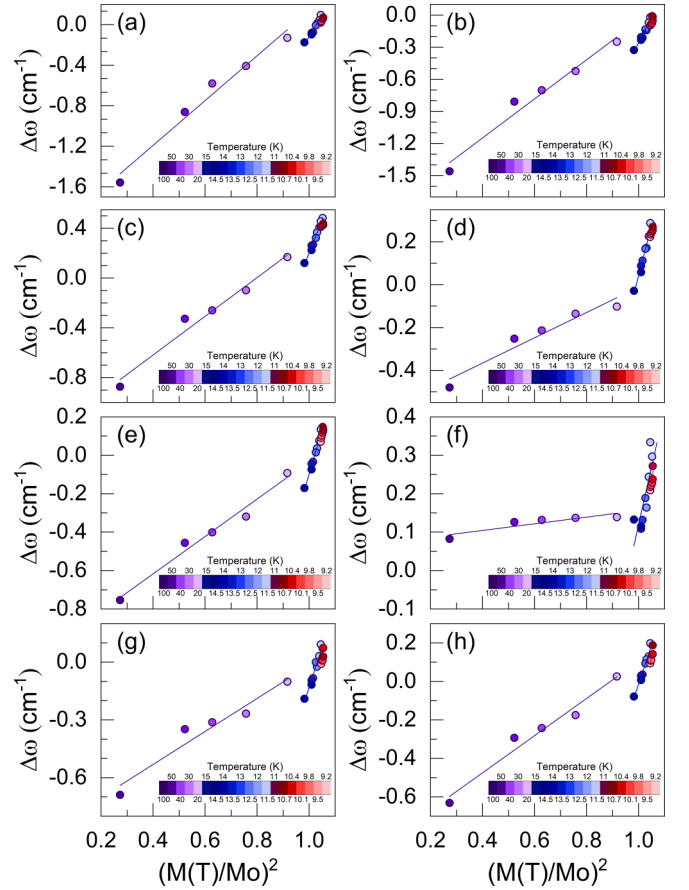
Figure 4 shows $\Delta\omega$ as a function of $[M(T)/M_0]^2$ for the selected phonons. The model, as expressed in Eq. (4), elucidates a direct linear correspondence between the phonon renormalization phenomenon and the adjustments in the gradient of the linear trend within distinct temperature intervals ($T^* > 15$ K; $T_N < T < T^*$; $T_N < T$). This correspondence firmly establishes the existence of SPC. Notably, the discernible alteration in the phonon behavior at T^* distinctly suggests the onset of SPC within CsCuCl$_3$. The slopes derived from SPC are summarized in Table SIII in the Supplemental Material [17]. These slope variations, evident in Fig. 4, are consistent with SPC-related materials such as Cu$_2$OCl$_2$ [62], thus robustly substantiating the presence of SPC in CsCuCl$_3$. This congruence bolsters the proposed models that underpin the correction of phonon energy renormalization, intensifying our confidence in the tangible manifestation of SPC within CsCuCl$_3$. As previously mentioned, the detected anomalies (occurring within the temperature range of $T_N < T < T^*$) in the low-temperature phonon dependence stand apart from any indications of lattice distortion, electronic phase transitions, or previously reported structural or magnetic phase transitions within the material. This distinct dissociation from these conventional factors suggests a potential antecedent magnetic
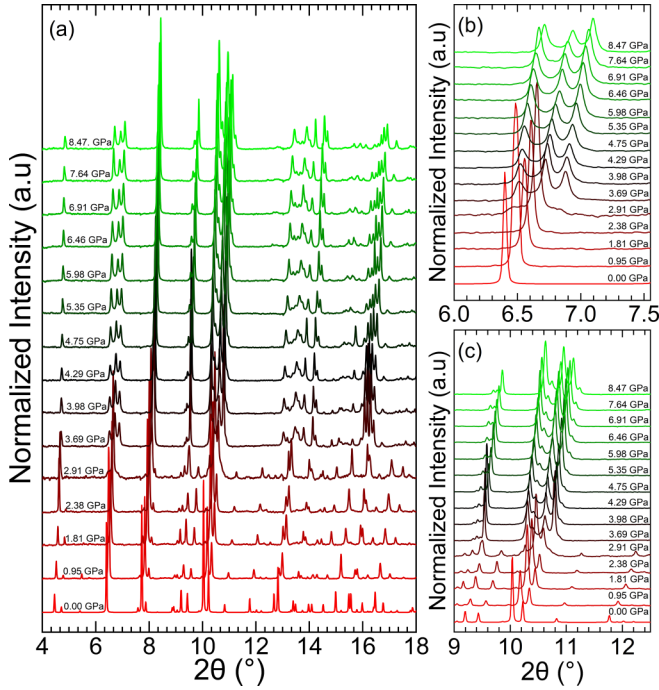
FIG. 5. (a) Pressure-dependent synchrotron powder x-ray diffraction (SPXRD) pattern of $CsCuCl_3$. (b) Pressure-dependent SPXRD pattern zoom around the 2θ (6–7.6 range). (c) Pressure-dependent SPXRD pattern zoom around the 2θ (9–13 range).

frustration effect, which appears to be concurrent with the onset of the observed SPC phenomenon.

C. Pressure-induced SPT on $CsCuCl_3$

As was previously discussed, $CsCuCl_3$ exhibits pressure-induced quantum phases, which enhance the neighboring spins in the sample and modify the magnetic diagram by the enhanced DM interaction [19,20]. Figure 5(a) shows the pressure-dependent SPXRD pattern obtained from $CsCuCl_3$. The diffraction patterns are well described by the same $P6_522$ structure up to 2.38 GPa. Above the critical pressure $P_c = 3.69$ GPa, the diffractograms exhibit abrupt changes, indicating the presence of new reflections, which can be attributed to a pressure-induced SPT. At around $P = 2.91$ GPa, both low-pressure (LP) and HP phases coexist. Remarkably, the emergence of new diffraction peaks, such as the splitting of the $6.6°$ band and the appearance of the distribution of the peak $\sim 10°$ [see Figs. 5(b) and 5(c)], indicates a decrease in symmetry of the HP phase. No remarkable changes in the diffraction patterns were detected up to 9 GPa, indicating that $CsCuCl_3$ does not undergo any other phase transition within the maximum pressure range explored in this paper.

All patterns of the LP phase were refined using the Rietveld method implemented in EXPO2014 software with the hexagonal $P6_522$ structure obtained from our SCXRD measurement. To investigate the crystal structure of the HP phase, primarily the x-ray powder pattern was compared with the one corresponding to the orthorhombic $CsCuBr_3$ ($C222_1$) structure reported in Ref. [63] (ICSD: 10184) as a possible solution.
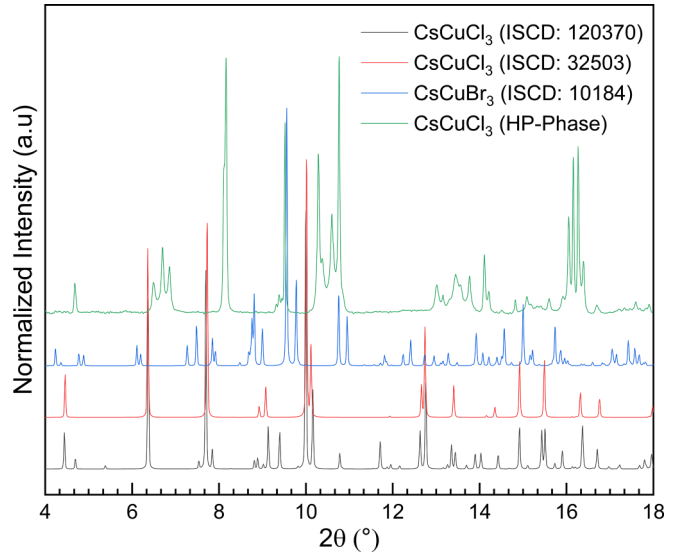

FIG. 6. Simulated diffraction patterns of the $CsCuCl_3$ ($P6_522$—ICSD: 120370), $CsCuCl_3$ ($P6_3/mmc$—ISCD: 32503), $CsCuBr_3$ ($C222_1$—ICSD: 10184), and the $CsCuCl_3$ synchrotron powder x-ray diffraction pattern obtained at 3.63 GPa.

However, the reflections of the simulated XRD patterns did not match the experimental data. Thus, our results differ from the high-temperature SPT [16,64,65], which involves a hexagonal-to-hexagonal $P6_122$ or $P6_522 \rightarrow P6_3/mmc$ at 423 K, and the HP hexagonal subcell ($P6_3/mmc$) encountered at 3.04 GPa by Christy *et al.* [66] (ISCD: 32503). A comparison of all diffractograms is provided in Fig. 6.

The HP phase was fitted by the Le Bail method using EXPO2014 software. The results suggest a base-centered monoclinic structure (type C). Unfortunately, the low diffraction intensity due to the sample texture and preferential orientation does not allow a high-quality number of peaks, which makes the diffractogram refinement challenging. As discussed before, $CsCuCl_3$ adopts the $P6_522$ [$a = b = 7.2168\,(10)$ Å, $c = 18.1853\,(5)$ Å] structure at room pressure with a threefold rotational symmetry along the principal c axis, with the copper (located at the center) and chlorine (vertices of the octahedron) atoms forming a distorted octahedron coordination geometry [$CuCl_6$] [35]. Each octahedron shares a common edge, forming a linear chain of octahedra that runs through the crystal structure along the principal axis. Cs^+ ions occupy the interstitial sites between the displayed chains.

Under HP, the structure undergoes the SPT to the monoclinic one [$a = 6.8875\,(12)$ Å, $b = 6.7918\,(2)$ Å, $c = 5.8539\,(10)$ Å, $\beta = 93.76\,(4)°$]. To facilitate the discussion of the relationship between both phases, a transformation was made on the crystal cell parameters: $a_h = a_m$; $\sqrt{3}b_h = b_m$; $c_h = 3c_m$ [67–69] (see Fig. S4 in the Supplemental Material [17]). Figure 7 shows the pressure dependence of the reduced unit cell parameters; a shift over all lattice parameters was observed, indicating crystal modification. The significant discontinuity indicates a first-order transition character.

The resulting structural distortion induced by the SPT can generate uniaxial stress as a function of the compound elastic
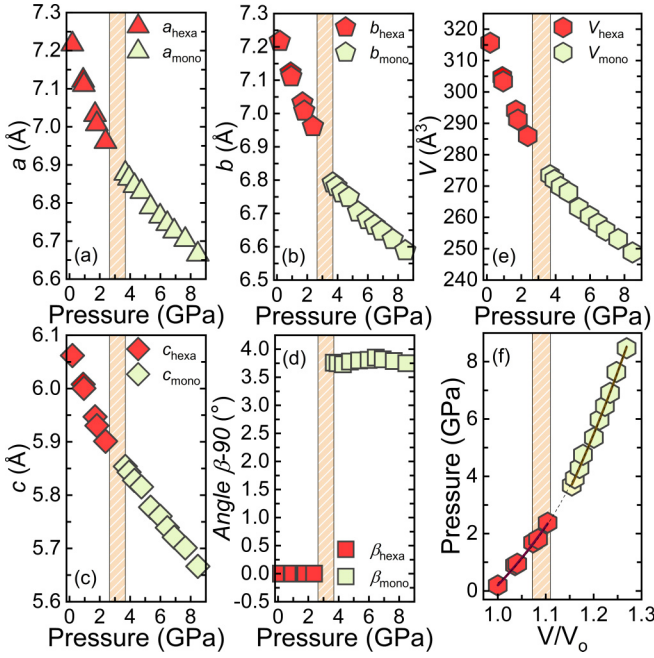
FIG. 7. (a)–(e) The lattice parameters as a function of pressure. (f) Third-order Birch-Murnaghan fit for each pressure phase. The orange region dashboard stands for the coexisting phases of both crystal structures.

anisotropy, which can be predicted by the equation of state (EOS) [70–72]. The third-order Birch-Murnaghan EOS was used to fit the pressure dependence of the unit cell volume [see Fig. 8(f)]. The equation was expressed in terms of the volume at zero pressure (V_0), the bulk modulus $B_0 = (-V\,\partial P/\partial V)_T$, and the dimensionless pressure derivative $B' = (\partial B/\partial P)_T$ (dimensionless), which describes, as B_0 changes with pressure

FIG. 8. (a) Pressure-dependent Raman spectra of CsCuCl₃. (b) Pressure dependence of the Raman mode positions. The orange region dashboard represents the coexisting low-pressure (LP)- and high-pressure (HP)-phase regions.

[73],

$$P = \frac{3}{2}B_0\left[\left(\frac{V_0}{V}\right)^{7/3} - \left(\frac{V_0}{V}\right)^{5/3}\right]$$
$$\times \left[1 + \frac{3}{4}(B'-4)\left\{\left(\frac{V_0}{V}\right)^{2/3} - 1\right\}\right]. \quad (5)$$

Table II shows the parameters obtained by the pressure-dependent unit cell volume fit using the third-order Birch-Murnaghan EOS. The SPT was accompanied by increased unit cell volume, which is consistent and expected for HP phases with higher bulk modulus due to their denser and less compressible crystal structure [74]. The B_0 values typically range from 10 to 70 GPa for hybrids/inorganic materials based on metal halide perovskites [75–80]. The low bulk modulus of metal halide perovskites is thought to contribute to their unique properties, such as self-healing, ion migration, and low thermal conductivity, which suggest applications in the flexible electronics industry for their ductility [81,82]. The value of B' indicates a slow stiffening of the material, which can be attributed to the first-order SPT, where both LP and HP phases can be related to a unique basic set. The presence of dynamic instability in the sample was not observed, and the positive value of B' compensated for any instability.

Since Raman spectra are sensitive to crystalline structure, we performed Raman spectroscopy in CsCuCl₃ at HP to gain insights into Raman-active modes and structural changes in CsCuCl₃ across different phases of the material correlated to SPXRD. Figure 8 shows the pressure-dependent Raman spectra of CsCuCl₃ up to 7 GPa. From room pressure up to 2.51 GPa, we can observe that the spectra keep the same Raman bands profile. Hence, a reorganization process involving the dimer unit [Cu₂Cl₉]⁵⁻ was observed in a 2.79–3.57 GPa range, where both LP and HP phases coexist, which means hexagonal and monoclinic phases. Consistent with SPXRD, a sudden change in the Raman spectra pressure-dependence modification is observed at 4.01 GPa, where new phonons are displayed in the Raman spectra, pertinent to a new crystalline phase. Thus, our Raman results confirm those obtained by diffraction.

Note that the pressure dependence of the phonons progressively becomes less resolved, probably due to stress induced along the SPT or could be a consequence of the increase in the sample bulk modulus. In general, the pressure dependence of the mode frequencies is linear. We observe this behavior in both phases. Furthermore, the Cl-Cu-Cl bending under pressure contributes more to the reorganization around the SPT for the number of displayed bands. However, the most intense band in the Raman spectra, the Cl-Cu-Cl stretching, is associated with the stronger distortion of [Cu₂Cl₉]⁵⁻ for the significant redshift. The Grüneisen parameters of each mode (see Table III) are given by

$$\gamma_{iT} = (B_0/\omega_i)(\partial\omega_i/\partial P)_T, \quad (6)$$

where B_0 is the bulk modulus of each phase, $(\partial\omega_i/\partial P)_T$ is the proper linear slope, and ω_i is the Raman frequency of the specific Grüneisen parameter (γ_{iT}) [83,84]. As predicted, the Cl-Cu-Cl bending modes have higher values of γ_{iT} than the Cu-Cl stretching, contributing to the modification in
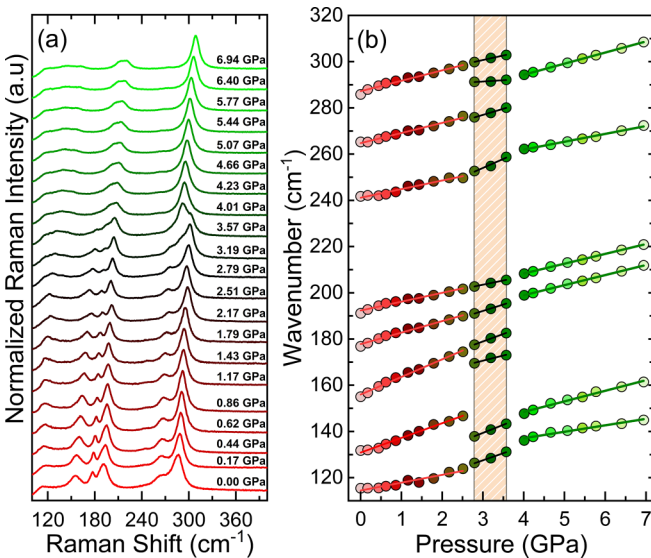
TABLE II. Experimental coefficients of the Birch-Murnaghan EOS for CsCuCl$_3$ in each structural phase.

Crystal system	P_{range} (GPa)	V_0 (Å^3)	B_0 (GPa)	B'
Hexagonal	0.10−2.38	319.42 ± 0.02	17 ± 3	4.39 ± 0.04
Monoclinic	3.69−8.47	304.62 ± 0.06	27 ± 9	4.26 ± 0.07

[Cu$_2$Cl$_9$]$^{5-}$. Comparing the phonon frequencies, the Cl-Cu-Cl stretching exhibits more significant shifts, consistent with previous predictions. This result establishes the structural correlations between bulk modulus and the corresponding local Grüneisen parameter. Confirming the XRD results, the Raman spectra show that, for pressures up to 9 GPa, the CsCuCl$_3$ material does not undergo amorphization.

Finally, this transition is reversible since the hexagonal phase was obtained again after the full release of pressure CsCuCl$_3$ (see Fig. S5 of the Supplemental Material [17]). However, it is important to point out that the critical pressure for the decompression cycle was lower than that obtained at the increasing process. The coexisting region could be responsible for the slow liberation of pressure and the readjustment to the original crystal structure. However, the recovery of the LP phase is well preserved. This is expected since the SPT is a first-order one.

IV. CONCLUSIONS

Investigating the SPTs and their related physical phenomena in halide perovskite materials under extreme conditions is significant for understanding their fundamental properties and exploring their potential applications in various fields. In the case of CsCuCl$_3$, applying low-temperature Raman spectroscopy has unveiled a distinct SPC mechanism. This coupling is evidenced by discernible shifts and broadening in the frequencies and FWHM of select phonons linked to Cl-Cu-Cl bending and stretching modes. This SPC generates an expected contribution to the phonon frequencies, observed at $T^* = 15$ K, suggesting a magnetic frustration within the material. This correlation between spin and phonon behaviors becomes more apparent with a discernible hardening of phonon temperature dependence around the anticipated

renormalization temperature $T_N = 10.7$ K, reflective of the underlying AFM effects. Utilizing $\Delta\omega$ as a function of $[M(T)/M_0]^2$ reinforces the discernible transformation linked to the SPC renormalization process at T^*.

Conversely, conducting HP investigations involving SPXRD and Raman spectroscopy on CsCuCl$_3$ has brought a first-order SPT at the critical pressure $P_c = 3.69$ GPa from the hexagonal $P6_522$ space group to the base-centered monoclinic type C cell. An intriguing feature emerges wherein the direct correlation in crystal axes engenders a gradual and natural crystal reconfiguration devoid of significant dynamic instability. This observation implies a degree of inherent flexibility within CsCuCl$_3$. Notably, the coexistence of phases is discernible within the pressure range from 2.79 to 3.57 GPa. The SPT involves the reorganization of the internal [Cu$_2$Cl$_9$]$^{5-}$ dimer unit, with Cl-Cu-Cl bending contributing more than Cl-Cu-Cl stretching. The prominent shift presence and highest γ_{iT} value associated with the displayed band indicates heightened distortion. Moreover, our analysis underscores the reversible nature of the SPT; however, residual strain pressure influences the modification of the P_c value upon pressure decrease. These findings supplied additional information about modifying [Cu$_2$Cl$_9$]$^{5-}$ under pressure and enhanced our understanding of the lattice distortion at external pressure.

TABLE III. Experimental Raman modes for CsCuCl$_3$ in each structural phase and their corresponding Grüneisen parameters. The material bulk modulus was $B_0 = 17$ and 27 GPa for each phase, obtained from the fit of the SPXRD pattern by the third-order Birch-Murnaghan equation.

LP phase			Coexistence phase			HP phase		
ω_i (cm^{-1})	$(\partial\omega_i/\partial P)_T$ (cm^{-1}/GPa)	γ_{iT}	ω_i (cm^{-1})	$(\partial\omega_i/\partial P)_T$ (cm^{-1}/GPa)	γ_{iT}	ω_i (cm^{-1})	$(\partial\omega_i/\partial P)_T$ (cm^{-1}/GPa)	γ_{iT}
–	–	–	109	6.2 ± 0.6	–	126	2.8 ± 0.2	0.6
114	3.4 ± 0.3	0.5	118	7.0 ± 0.2	–	130	4.6 ± 0.2	1.0
131	6.3 ± 0.2	0.8	157	4.5 ± 0.8	–	–	–	–
156	7.6 ± 0.2	0.8	160	6.5 ± 0.4	–	–	–	–
178	5.0 ± 0.2	0.5	176	5.5 ± 0.3	–	182	4.4 ± 0.1	0.7
192	3.8 ± 0.2	0.3	193	3.6 ± 0.1	–	191	4.2 ± 0.1	0.6
241	3.7 ± 0.3	0.3	231	7.8 ± 0.9	–	248	3.4 ± 0.1	0.4
265	4.4 ± 0.2	0.3	261	5.3 ± 0.4	–	–	–	–
–	–	–	288	1.1 ± 0.5	–	275	4.8 ± 0.1	0.5
287	4.5 ± 0.3	0.3	289	3.9 ± 0.3	–	–	–	–

[1] R. Roccanova, A. Yangui, G. Seo, T. D. Creason, Y. Wu, D. Y. Kim, M. H. Du, and B. Saparov, Bright luminescence from nontoxic CsCu$_2X_3$ (X = Cl, Br, I), ACS Mater. Lett. **1**, 459 (2019).

[2] F. Cao and L. Li, Progress of lead-free halide perovskites: from material synthesis to photodetector application, Adv. Funct. Mater. **31**, 2008275 (2021).

[3] X. Zhang, B. Zhou, X. Chen, and W. W. Yu, Reversible transformation between Cs$_3$Cu$_2$I$_5$ and CsCu$_2$I$_3$ perovskite derivatives and its anticounterfeiting application, Inorg. Chem. **61**, 399 (2022).

[4] Y. Lu, G. Li, S. Fu, S. Fang, and L. Li, CsCu$_2$I$_3$ nanocrystals: Growth and structural evolution for tunable light emission, ACS Omega **6**, 544 (2021).

[5] M. ben Bechir and M. H. Dhaou, Study of charge transfer mechanism and dielectric relaxation of CsCuCl$_3$ perovskite nanoparticles, Mater. Res. Bull. **144**, 111473 (2021).

[6] Y. Zheng, X. Yuan, J. Yang, Q. Li, X. Yang, Y. Fan, H. Li, H. Liu, and J. Zhao, Cu doping-enhanced emission efficiency of Mn^{2+} in cesium lead halide perovskite nanocrystals for efficient white light-emitting diodes, J. Lumin. **227**, 117586 (2020).

[7] R. Wu, Z. Bai, J. Jiang, H. Yao, and S. Qin, Research on the photoluminescence properties of Cu^{2+}-doped perovskite CsPbCl$_3$ quantum dots, RSC Adv. **11**, 8430 (2021).

[8] J. S. Rodríguez-Hernández, M. A. P. Gómez, D. S. Abreu, A. Nonato, R. X. da Silva, A. García-Fernández, M. A. Señarís-Rodríguez, M. Sánchez-Andújar, A. P. Ayala, and C. W. A. Paschoal, Uniaxial negative thermal expansion in the [(CH$_3$)$_2$NH$_2$]PbBr$_3$ hybrid perovskite, J. Mater. Chem. C Mater. **10**, 17567 (2022).

[9] L. T. Nguyen and R. J. Cava, Hexagonal perovskites as quantum materials, Chem. Rev. **121**, 2935 (2021).

[10] S. Fop, K. S. McCombie, E. J. Wildman, J. M. S. Skakle, and A. C. Mclaughlin, Hexagonal perovskite derivatives: A new direction in the design of oxide ion conducting materials, Chem. Commun. **55**, 2127 (2019).

[11] L. Balents, Spin liquids in frustrated magnets, Nature (London) **464**, 199 (2010).

[12] J. Collocott and J. A. Rayne, Low-temperature heat capacity of linearachain magnetic compounds CsNiCl$_3$, RbNiCl$_3$, and CsCuCl$_3$, J. Appl. Phys. **61**, 4404 (1987).

[13] A. Miyake, J. Shibuya, M. Akaki, H. Tanaka, and M. Tokunaga, Magnetic field induced polar phase in the chiral magnet CsCuCl$_3$, Phys. Rev. B **92**, 100406(R) (2015).

[14] H. Ueda, E. Skoropata, M. Burian, V. Ukleev, G. S. Perren, L. Leroy, J. Zaccaro, and U. Staub, Conical spin order with chiral quadrupole helix in CsCuCl$_3$, Phys. Rev. B **105**, 144408 (2022).

[15] V. P. Plakhty, J. Wosnitza, N. Martin, Y. Marchi, O. P. Smirnov, B. Grenier, and S. V. Gavrilov, Isostructural transition coupled with spin ordering in CsCuCl$_3$: A spatially frustrated spiral crystal lattice, Phys. Rev. B **79**, 012410 (2009).

[16] C. J. Kroese and W. J. A. Maaskant, The relation between the high-temperature and room-temperature structure of CsCuCl$_3$, Chem. Phys. **5**, 224 (1974).

[17] See Supplemental Material at http://link.aps.org/supplemental/10.1103/PhysRevB.109.054116 for a detailed view of the two possible crystalline structures of CsCuCl$_3$; details of the group factor analysis of the CsCuCl$_3$ crystal structure at room pressure; high-resolution Raman spectra of CsCuCl$_3$ at 300 K fitted with Lorentzians; a detailed list of phonons in CsCuCl$_3$ calculated by DFPT; temperature dependence of phonon frequencies and FWHM for selected phonons; temperature-dependent Raman spectra of CsCuCl$_3$ using λ = 514 nm radiation and temperature dependence of selected phonons frequencies; anharmonic contributions to the frequencies with the FWHMs of selected phonons; the crystal phase transformation basic sets along the pressure-induced phase transition; and the pressure-dependent Raman spectra of CsCuCl$_3$ along decompression.

[18] K. Nihongi, T. Kida, Y. Narumi, J. Zaccaro, Y. Kousaka, K. Inoue, K. Kindo, Y. Uwatoko, and M. Hagiwara, Magnetic field and pressure phase diagrams of the triangular-lattice antiferromagnet CsCuCl$_3$ explored via magnetic susceptibility measurements with a proximity-detector oscillator, Phys. Rev. B **105**, 184416 (2022).

[19] A. Sera, Y. Kousaka, J. Akimitsu, M. Sera, and K. Inoue, Pressure-induced quantum phase transitions in the $S = \frac{1}{2}$ triangular lattice antiferromagnet CsCuCl$_3$, Phys. Rev. B **96**, 014419 (2017).

[20] M. Hosoi, H. Matsuura, and M. Ogata, New magnetic phases in the chiral magnet CsCuCl$_3$ under high pressures, J. Phys. Soc. Jpn. **87**, 075001 (2018).

[21] D. Yamamoto, T. Sakurai, R. Okuto, S. Okubo, H. Ohta, H. Tanaka, and Y. Uwatoko, Continuous control of classical-quantum crossover by external high pressure in the coupled chain compound CsCuCl$_3$, Nat. Commun. **12**, 4263 (2021).

[22] Y. Liu, Q. Liu, Y. Liu, X. Jiang, X. Zhang, and J. Zhao, Effects of spin-phonon coupling on two-dimensional ferromagnetic semiconductors: A case study of iron and ruthenium trihalides, Nanoscale **13**, 7714 (2021).

[23] B. H. Zhang, Y. S. Hou, Z. Wang, and R. Q. Wu, First-principles studies of spin-phonon coupling in monolayer Cr$_2$Ge$_2$Te$_6$, Phys. Rev. B **100**, 224427 (2019).

[24] G. Qin, H. Wang, L. Zhang, Z. Qin, and M. Hu, Giant effect of spin-lattice coupling on the thermal transport in two-dimensional ferromagnetic CrI$_3$, J. Mater. Chem. C Mater. **8**, 3520 (2020).

[25] D. Pesin and L. Balents, Mott physics and band topology in materials with strong spin-orbit interaction, Nat. Phys. **6**, 376 (2010).

[26] C. H. Sohn, C. H. Kim, L. J. Sandilands, N. T. M. Hien, S. Y. Kim, H. J. Park, K. W. Kim, S. J. Moon, J. Yamaura, Z. Hiroi *et al.*, Strong spin-phonon coupling mediated by single ion anisotropy in the all-in-all-out pyrochlore magnet $Cd_2Os_2O_7$, Phys. Rev. Lett. **118**, 117201 (2017).

[27] J. Son, B. C. Park, C. H. Kim, H. Cho, S. Y. Kim, L. J. Sandilands, C. Sohn, J. G. Park, S. J. Moon, and T. W. Noh, Unconventional spin-phonon coupling via the Dzyaloshinskii-Moriya interaction, npj Quantum Mater. **4**, 17 (2019).

[28] L. Krause, R. Herbst-Irmer, G. M. Sheldrick, and D. Stalke, Comparison of silver and molybdenum microfocus x-ray sources for single-crystal structure determination, J. Appl. Cryst. **48**, 3 (2015).

[29] A. L. Spek, Single-crystal structure validation with the program PLATON, J. Appl. Cryst. **36**, 7 (2003).

[30] G. M. Sheldrick, SHELXT—Integrated space-group and crystal-structure determination research papers, Acta Cryst. A **71**, 3 (2015).

[31] G. M. Sheldrick, Crystal structure refinement with SHELXL, Acta Cryst. C **71**, 3 (2015).

[32] O. V. Dolomanov, L. J. Bourhis, R. J. Gildea, J. A. K. Howard, and H. Puschmann, OLEX2: A complete structure solution, refinement and analysis program, J. Appl. Cryst. **42**, 339 (2009).

[33] C. F. Macrae, I. Sovago, S. J. Cottrell, P. T. A. Galek, E. Pidcock, M. Platings, G. P. Shields, J. S. Stevens, M. Towler, and P. A. Wood, Mercury 4.0: From visualization to analysis, design and prediction, J. Appl. Cryst. **53**, 226 (2020).

[34] K. Momma and F. Izumi, VESTA 3 for three-dimensional visualization of crystal, volumetric and morphology data, J. Appl. Cryst. **44**, 1272 (2011).

[35] S. Cui, Y. Chen, S. Tao, J. Cui, C. Yuan, N. Yu, H. Zhou, J. Yin, and X. Zhang, Synthesis, crystal structure and photoelectric response of all-inorganic copper halide salts $CsCuCl_3$, Eur. J. Inorg. Chem. **2020**, 2165 (2020).

[36] G. Shen, Y. Wang, A. Dewaele, C. Wu, D. E. Fratanduono, J. Eggert, S. Klotz, K. F. Dziubek, P. Loubeyre, O. V. Fat'yanov *et al.*, Toward an international practical pressure scale: A proposal for an IPPS ruby gauge (IPPS-Ruby2020), High Press. Res. **40**, 299 (2020).

[37] M. Wojdyr, FITYK: A general-purpose peak fitting program, J. Appl. Cryst. **43**, 1126 (2010).

[38] C. Prescher and V. B. Prakapenka, DIOPTAS: A program for reduction of two-dimensional x-ray diffraction data and data exploration, High Press. Res. **35**, 223 (2015).

[39] A. Boultif and D. Louër, Powder pattern indexing with the dichotomy method, J. Appl. Cryst. **37**, 724 (2004).

[40] A. Altomare, C. Cuocci, C. Giacovazzo, A. Moliterni, R. Rizzi, N. Corriero, and A. Falcicchio, EXPO2013: A kit of tools for phasing crystal structures from powder data, J. Appl. Cryst. **46**, 1231 (2013).

[41] P. Giannozzi, S. Baroni, N. Bonini, M. Calandra, R. Car, C. Cavazzoni, D. Ceresoli, G. L. Chiarotti, M. Cococcioni, I. Dabo *et al.*, QUANTUM ESPRESSO: A modular and open-source software project for quantum simulations of materials, J. Phys.: Condens. Matter **21**, 395502 (2009).

[42] P. Giannozzi, O. Andreussi, T. Brumme, O. Bunau, M. B. Nardelli, M. Calandra, R. Car, C. Cavazzoni, D. Ceresoli, M. Cococcioni *et al.*, Advanced capabilities for materials modelling with QUANTUM ESPRESSO, J. Phys.: Condens. Matter **29**, 465901 (2017).

[43] D. R. Hamann, Optimized norm-conserving Vanderbilt pseudopotentials, Phys. Rev. B **88**, 085117 (2013); **95**, 239906(E) (2017).

[44] J. P. Perdew, K. Burke, and M. Ernzerhof, Generalized gradient approximation made simple, Phys. Rev. Lett. **78**, 1396(E) (1997).

[45] J. Petzelt, I. Gregora, V. Vorliiiek, J. Fousek, B. Biezina, G. V. Kozlov, and A. A. Volkov, Far-infrared and Raman spectroscopy of the phase transition in $CsCuCl_3$, J. Raman Spectrosc. **10**, 187 (1981).

[46] G. M. Cole Jr., C. F. Putnik, and S. L. Holt, Physical properties of linear-chain systems. II. Optical spectrum of $CsMnBr_3$, Inorg. Chem. **14**, 2219 (1975).

[47] U. Kambli and H. U. Giidel, Optical absorption and luminescence studies of antiferromagnetic $RbMnCl_3$ and $CsMnCl_3$, J. Phys. C: Solid State Phys. **17**, 4041 (1984).

[48] C. W. Tomblin, G. D. Jones, and R. W. G. Syme, Raman scattering and infrared absorption spectra of Co^{2+} ions in $CsMgBr_3$ and $CsCdBr_3$, J. Phys. C: Solid State Phys **17**, 4345 (1984).

[49] E. Jara, J. A. Barreda-Argüeso, J. González, F. Rodríguez, and R. Valiente, Origin of the piezochromism in Cs_2CuCl_4: Electron-phonon and crystal-structure correlations, Phys. Rev. B **99**, 134106 (2019).

[50] L. Nataf, F. Aguado, I. Hernández, R. Valiente, J. González, M. N. Sanz-Ortiz, H. Wilhelm, A. P. Jephcoat, F. Baudelet, and F. Rodríguez, Volume and pressure dependences of the electronic, vibrational, and crystal structures of Cs_2CoCl_4: Identification of a pressure-induced piezochromic phase at high pressure, Phys. Rev. B **95**, 014110 (2017).

[51] Y. Rodríguez-Lazcano, L. Nataf, and F. Rodríguez, Electronic structure and luminescence of $[(CH_3)_4N]_2MnX_4(X = Cl, Br)$ crystals at high pressures by time-resolved spectroscopy: Pressure effects on the Mn-Mn exchange coupling, Phys. Rev. B **80**, 085115 (2009).

[52] N. Nakagawa, N. Abe, S. Toyoda, S. Kimura, J. Zaccaro, I. Gautier-Luneau, D. Luneau, Y. Kousaka, A. Sera, M. Sera *et al.*, Magneto-chiral dichroism of $CsCuCl_3$, Phys. Rev. B **96**, 121102(R) (2017).

[53] D. J. Lockwood and M. G. Cottam, The spin-phonon interaction in FeF_2 and MnF_2 studied by Raman spectroscopy, J. Appl. Phys. **64**, 5876 (1988).

[54] L. Du, J. Tang, Y. Zhao, X. Li, R. Yang, X. Hu, X. Bai, X. Wang, K. Watanabe, T. Taniguchi *et al.*, Lattice dynamics, phonon chirality, and spin-phonon coupling in 2D itinerant ferromagnet Fe_3GeTe_2, Adv. Funct. Mater. **29**, (2019).

[55] E. Aytan, B. Debnath, F. Kargar, Y. Barlas, M. M. Lacerda, J. X. Li, R. K. Lake, J. Shi, and A. A. Balandin, Spin-phonon coupling in antiferromagnetic nickel oxide, Appl. Phys. Lett. **111**, 252402 (2017).

[56] R. X. Silva, H. Reichlova, X. Marti, D. A. B. Barbosa, M. W. Lufaso, B. S. Araujo, A. P. Ayala, and C. W. A. Paschoal, Spin-phonon coupling in $Gd(Co_{1/2}Mn_{1/2})O_3$ perovskite, J. Appl. Phys. **114**, 194102 (2013).

[57] A. F. García-Flores, E. Granado, H. Martinho, C. Rettori, E. I. Golovenchits, V. A. Sanina, S. B. Oseroff, S. Park, and S. W. Cheong, Magnetically frustrated behavior in multiferroics RMn_2O_5 $(R = Bi, Eu, and Dy)$: A Raman scattering study, J. Appl. Phys. **101**, 09M106 (2007).

[58] A. F. García-Flores, E. Granado, H. Martinho, R. R. Urbano, C. Rettori, E. I. Golovenchits, V. A. Sanina, S. B. Oseroff, S.

Park, and S. W. Cheong, Anomalous phonon shifts in the paramagnetic phase of multiferroic RMn$_2$O$_5$ (R = Bi, Eu, Dy): Possible manifestations of unconventional magnetic correlations, Phys. Rev. B **73**, 104411 (2006).

[59] M. A. Prosnikov, A. N. Smirnov, V. Y. Davydov, R. V. Pisarev, N. A. Lyubochko, and S. N. Barilo, Magnetic dynamics and spin-phonon coupling in the antiferromagnet Ni$_2$NbBO$_6$, Phys. Rev. B **98**, 104404 (2018).

[60] B. Araújo, A. M. Arévalo-López, C. C. Santos, J. P. Attfield, C. W. A. Paschoal, and A. P. Ayala, Spin-phonon coupling in monoclinic BiCrO$_3$, J. Appl. Phys. **2020**, 114102 (2020).

[61] E. Granado, A. Garcí, J. A. Sanjurjo, C. Rettori, I. Torriani, F. Prado, R. D. Sá Nchez, A. Caneiro, and S. B. Oseroff, Magnetic ordering effects in the Raman spectra of La$_{1-x}$Mn$_{1-x}$O$_3$, Phys. Rev. B **60**, 11879 (1999).

[62] B. S. Araújo, A. M. Arévalo-López, J. P. Attfield, C. W. A. Paschoal, and A. P. Ayala, Spin-phonon coupling in melanothallite Cu$_2$OCl$_2$, Appl. Phys. Lett. **113**, 222901 (2018).

[63] T.-I. Li and G. D. Stucky, Exchange interactions in polynuclear transition metal complexes, structural properties of cesium tribromocuprate(II), CsCuBr$_3$, a strongly coupled copper(I1) system, Inorg. Chem. **12**, 441 (1973).

[64] C. J. Kroese, W. J. A. Maaskant, and G. C. Verschoor, The high-temperature structure of CsCuCl$_3$, Acta Cryst. B **30**, 1053 (1974).

[65] W. J. A. Masskant, On helices resulting from a cooperative Jahn-Teller effect in hexagonal perovskites, in *Iron-Sulfur Proteins Perovskites. Structure and Bonding* (Springer, Berlin, 1995), Vol. 83, pp. 55–87.

[66] A. G. Christy, R. J. Angel, J. Hainest, and S. M. Clark, Crystal structural variation and phase transition in caesium trichlorocnprate at high pressure, J. Phys.: Condens. Matter **6**, 3125 (1994).

[67] S. Ivantchev, E. Kroumova, G. Madariaga, J. M. Pérez-Mato, and M. I. Aroyo, SUBGROUPGRAPH: A computer program for analysis of group-subgroup relations between space groups, J. Appl. Cryst. **33**, 1190 (2000).

[68] E. Kroumova, M. L. Aroyo, J. M. Perez-Mato, A. Kirov, C. Capillas, S. Ivantchev, and H. Wondratschek, Bilbao Crystallographic Server: Useful databases and tools for phase-transition studies, Phase Transit. **76**, 155 (2003).

[69] G. De La Flor, D. Orobengoa, E. Tasci, J. M. Perez-Mato, and M. I. Aroyo, Comparison of structures applying the tools available at the Bilbao Crystallographic Server, J. Appl. Cryst. **49**, 653 (2016).

[70] F. Birch, Finite elastic strain of cubic crystals, Phys. Rev. **71**, 809 (1947).

[71] N. Sata, G. Shen, M. L. Rivers, and S. R. Sutton, Pressure-volume equation of state of the high-pressure $B2$ phase of NaCl, Phys. Rev. B **65**, 104114 (2002).

[72] A. L. Goodwin, D. A. Keen, and M. G. Tucker, Large negative linear compressibility of Ag$_3$[Co(CN)$_6$], Proc. Natl. Acad. Sci. USA **105**, 18708 (2008).

[73] T. Katsura and Y. Tange, A simple derivation of the Birch-Murnaghan equations of state (EOSs) and comparison with EOSs derived from other definitions of finite strain, Minerals **9**, 745 (2019).

[74] V. Svitlyk, D. Chernyshov, A. Bosak, E. Pomjakushina, A. Krzton-Maziopa, K. Conder, V. Pomjakushin, V. Dmitriev, G. Garbarino, and M. Mezouar, Compressibility and pressure-induced disorder in superconducting phase-separated Cs$_{0.72}$Fe$_{1.57}$Se$_2$, Phys. Rev. B **89**, 144106 (2014).

[75] R. O. Agbaoye, P. O. Adebambo, and G. A. Adebayo, First principles comparative studies of thermoelectric and other properties in the cubic and hexagonal structure of CsCdCl$_3$ halide perovskites, Comput. Condens. Matter **21**, e00388 (2019).

[76] Q. Tu, D. Kim, M. Shyikh, and M. G. Kanatzidis, Mechanics-coupled stability of metal-halide perovskites, Matter **4**, 2765 (2021).

[77] M. Mączka, S. Sobczak, P. Ratajczyk, F. F. Leite, W. Paraguassu, F. Dybała, A. P. Herman, R. Kudrawiec, and A. Katrusiak, Pressure-driven phase transition in two-dimensional perovskite MHy$_2$PbBr$_4$, Chem. Mater. **34**, 7867 (2022).

[78] L. Zhang, L. Wang, K. Wang, and B. Zou, Pressure-induced structural evolution and optical properties of metal-halide perovskite CsPbCl$_3$, J. Phys. Chem. C **122**, 15220 (2018).

[79] L. Zhang, Q. Zeng, and K. Wang, Pressure-induced structural and optical properties of inorganic halide perovskite CsPbBr$_3$, J. Phys. Chem. Lett. **8**, 3752 (2017).

[80] W. Castro Ferreira, B. S. Araújo, M. A. P. Gómez, F. E. O. Medeiros, C. W. A. Paschoal, C. B. Silva, P. T. C. Freire, U. F. Kaneko, F. M. Ardito, N. M. Souza-Neto *et al.*, Pressure-induced structural and optical transitions in luminescent bulk Cs$_4$PbBr$_6$, J. Phys. Chem. C **126**, 541 (2022).

[81] S. Sun, Y. Fang, G. Kieslich, T. J. White, and A. K. Cheetham, Mechanical properties of organic-inorganic halide perovskites, CH$_3$NH$_3$PbX$_3$ (X = I, Br and Cl), by nanoindentation, J. Mater. Chem. A Mater. **3**, 18450 (2015).

[82] Y. Rakita, S. R. Cohen, N. K. Kedem, G. Hodes, and D. Cahen, Mechanical properties of APbX$_3$ (A = Cs or CH$_3$NH$_3$; X = I or Br) perovskite single crystals, MRS Commun. **5**, 623 (2015).

[83] T. R. Ravindran, A. K. Arora, and T. A. Mary, High pressure behavior of ZrW$_2$O$_8$: Grüneisen parameter and thermal properties, Phys. Rev. Lett. **84**, 3879 (2000).

[84] F. D. Stacey and J. H. Hodgkinson, Thermodynamics with the Grüneisen parameter: Fundamentals and applications to high pressure physics and geophysics, Phys. Earth Planet. Inter. **286**, 42 (2019).